Disentangling bulk from surface contributions in the electronic structure of black phosphorus

E. Golias, M. Krivenkov, and J. Sánchez-Barriga

Helmholtz-Zentrum Berlin für Materialien und Energie, Elektronenspeicherring BESSY II, Albert-Einstein-Straße 15, 12489 Berlin, Germany

Most recently, black phosphorus has come into focus as a promising material for future applications in nanoelectronic devices due to its unique electronic and transport properties. Here, we use angle-resolved photoemission spectroscopy in conjunction with *ab initio* calculations within the framework of density-functional theory to disentangle surface from the bulk contributions in the electronic structure of black phosphorus. We find good agreement between our theoretical predictions for the intra- and interlayer energy-momentum dispersions and the experimentally obtained three-dimensional band structure of this material. Our results provide compelling evidence for the existence of surface-resonant states near the top of the valence band, which can play an important role in the performance of electronic devices based on black phosphorus.

I. INTRODUCTION

The advent of graphene [1–3] paved the way for the investigation of numerous layered two-dimensional (2D) materials [4,5] with prospective applications in optoelectronic devices. Graphene has remarkable transport characteristics [6]; however, its intrinsic semimetallic nature and the difficulty to open a band gap at the Dirac point while preserving its unique electronic properties [7] could hinder the introduction of graphene in logic applications. Most recently, transition-metal dichalcogenides (TMDs), which are intrinsically semi-conducting, have been proposed as an alternative and are currently under the spotlight for integration in optoelectronic devices [8–12]. TMDs comprise a plethora of layered 2D structures with band gap values between 1 and 2 eV that have already given encouraging results in actual field-effect transistors (FETs) [13–15].

Recently, the list of layered 2D structures has been extended by the second elemental laminar material after graphite, namely black phosphorus (BP) [16]. BP, the most stable allotrope of phosphorus, consists of puckered honeycomb monolayers (known as phosphorene) held together by Van der Waals (VdW) interlayer forces. Despite the fact that BP has been discovered over a century ago, it has attracted the community's attention only recently [17]. Fascinating physics can be realized in this system, primarily arising from the existence of a superconducting transition under pressure [18], strain-induced gap modifications [19], and semiconductor to Dirac semimetal [20,21] or semiconductor to topological quantum-phase transition [22] under an applied electric field. Most importantly, the unique electronic and transport properties of BP drive the resurgent interest on this material [23]. BP is a versatile semiconducting material with tunable band gap, which changes inversely proportional to the number of stacked monolayers. The band gap is always direct with a value of 1.5–2 eV [24,25] for phosphorene down to 0.3 eV [26–28] for the bulk BP reduced due to the interlayer interaction. The tunable band gap is valuable for optical devices but also for creating heterostructures with other 2D materials, such as TMDs or graphene. Another important knob in designing logic devices, the work function, also varies with the number of BP layers [29], allowing the modulation of carrier injection via Schottky-barrier tuning. Moreover,

BP shows strongly anisotropic optical [30] and electronic properties [31] along with hole-dominated ambipolar transport characteristics [32,33]. FETs based on BP have already given very good results with high on-off current ratios [34] and carrier mobilities [34,35] that can rival state-of-the-art devices based on TMDs.

In modern nanoelectronics, where the bulk-to-surface ratio is being reduced progressively, surface effects like surface states and resonances have a profound impact on the electrical and optical device characteristics. For instance, surface states are linked to detrimental device effects like mobility degradation and Fermi-level pinning [36]. But even in the bulk regime, transport in BP-based FETs channels can be confined in two dimensions [37–39], rendering surface effects a major factor in device performance. In this context, angle-resolved photoemission spectroscopy (ARPES) is a valuable tool that allows us to disentangle surface from bulk contributions. Moreover, it is the ultimate technique to bench-mark the effectiveness of current theoretical approaches to accurately describe the three-dimensional (3D) band structure of BP, which is strongly connected to several properties of the material-related applications. Early ARPES studies by Takahashi and coworkers [40] reported that, apart from small deviations, theoretical calculations [41] can describe consistently the electrons in bulk BP. On the contrary, a recent high-resolution photoemission study [42] suggested that theoretical methodologies [41,43–45] cannot fully describe important electronic properties of BP. For example, a strong renormalization in the upper part of the valence band has been reported, hence, rendering the electronic behavior of BP more 2D than theory predicts. In this respect, high-resolution band mapping using ARPES is crucial to determine the electronic behavior of BP and to test the accuracy of theoretical methodologies.

In the present work, we employ high-resolution ARPES in conjunction with *ab initio* calculations to provide compelling evidence for the existence of several intrinsic surface-resonant states in the electronic structure of BP. Furthermore, by carefully comparing the experimentally obtained electronic band dispersions to the theoretical results, we provide further insight about the charge carrier behavior along the intra- and interlayer directions. Our results are of critical importance
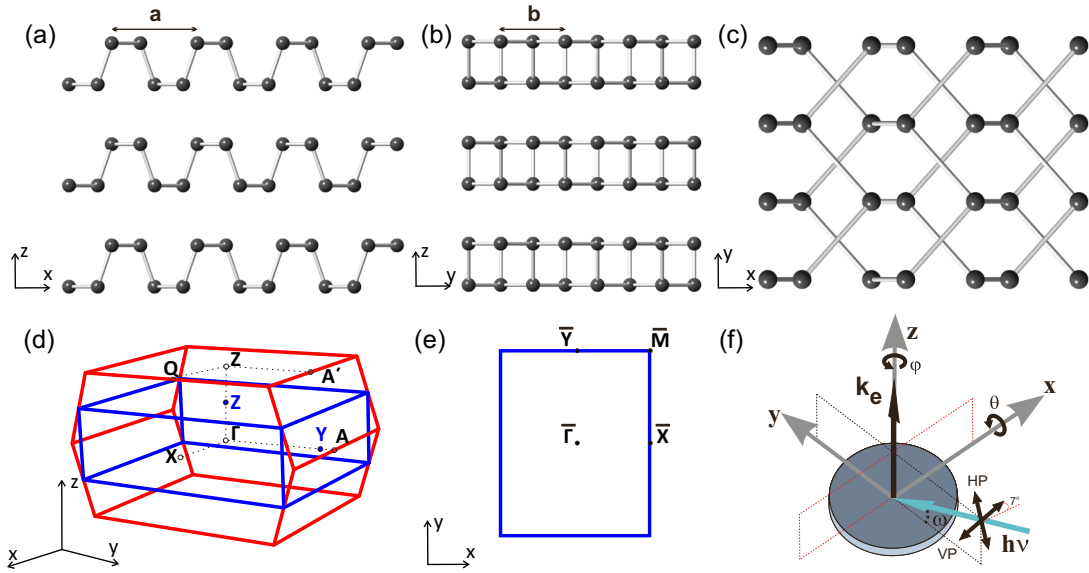
FIG. 1. Ball and stick model of the optimized crystal structure of bulk BP viewed from the (a) zigzag, (b) armchair, and (c) top perspective, respectively. (d) First BZ of bulk BP in the primitive base-centered orthorhombic (red) and conventional orthorhombic setup (blue), respectively. Black letters label high-symmetry points corresponding to the reciprocal space of the primitive cell and high-symmetry points that differ in the conventional setup are marked by blue letters. (e) Surface BZ projected along the [001] high-symmetry direction, which corresponds to the direction parallel to the BP surface. (f) Setup of the photoemission experiment in the sample reference frame; black and red dashed lines indicate the incidence plane and the analyzer slit, respectively.

in understanding the relative contributions from surface and bulk states near the Fermi level in BP, an aspect that might prove crucial to developing electronic devices of superior functionality based on this material.

II. METHODS

High-resolution ARPES measurements were performed at room temperature at the UE112-PGM2a beamline of BESSY II using a Scienta R8000 hemispherical electron analyzer and the experimental geometry illustrated in Fig. 1(f). We used vertical (VP) and horizontal (HP) linearly polarized light incident on the sample at an angle $\omega \approx 45°$ with respect to the surface normal. Thus, in the sample's reference frame, the light had a mixed $p + s$ or mainly s character for HP or VP light, respectively. By changing the angle of incidence, the character of the HP light was tuned between more p like for grazing incidence to more s like for $\omega \approx 90°$. Moreover, the light impinged the sample with a $7°$ tilt [see Fig. 1(f)]. We used photon energies between 65 and 130 eV, along with variable polarization in order to exploit the intensity modulations in the measured spectra due to the matrix-element effects. The energy and angular resolution of our experiments were $\sim$30 meV and $0.1°$, respectively. We used commercially available BP bulk single crystals [46], which were cleaved *in situ* under a base pressure lower than $\sim 1 \times 10^{-10}$ mbar. All subsequent APRES spectra were also acquired under the same conditions.

Theoretical calculations were performed within the DFT formalism using the projector-augmented wave method [47] and a semilocal exchange-correlation potential as implemented by Perdew, Burke, and Ernzerhof (PBE) [48]. The valence electrons were expanded in a plane-wave basis with kinetic energy up to 400 eV, and the nonlocal dispersive VdW

interactions were simulated using the DFT-D2 methodology of Grimme [49]. The reciprocal space was sampled with a Monkhorst-pack grid of $8 \times 10 \times 3$ for the bulk system in the conventional unit cell and scaled to preserve the same k-point density when the primitive cell was employed [see Fig. 4(d)]. A mesh of $8 \times 10 \times 1$ k points was used in the calculation of 1-, 2-, 3-, and 11-monolayer slabs in a configuration with a vacuum region larger than 20 Å separating the opposite surfaces in all cases. The structures were allowed to relax until the residual forces on phosphorus atoms were smaller than 10^{-3} eV/Å. The band structure calculations were performed using the hybrid functional HSE06 [50] with 25% of exact exchange except for the 11-monolayer slab where only the semilocal (PBE) functional was used as the exchange-correlation potential.

III. RESULTS AND DISCUSSION

Figures 1(a)–1(c) illustrate the optimized structure of bulk BP. The unit cell of BP comprises a base-centered orthorhombic lattice classified in the point group *Cmca*. The anisotropic nature of BP is clearly observed in its crystal structure along the basal high-symmetry directions, namely the armchair and the zigzag direction along the x and y axis, respectively. Table I tabulates the structural parameters of few-layer and bulk BP, as calculated using DFT, where we can see that the interlayer interaction reduces the lattice constant along the armchair direction as the number of stacked monolayers increases while the zigzag direction remains virtually constant. In Figs. 2(a)–2(c) we present the evolution of the electronic band structure as the number of BP layers increases up to the bulk limit [see Fig. 2(d)]. The interlayer interaction induces a reduction in the band-gap of BP at the $\bar{\Gamma}$ point of the surface

TABLE I. Calculated lattice constants for bulk and few-layer BP using a PBE exchange-correlation potential [48] and the method of Grimme [49] for the calculation of long-range VdW interactions.

	a (Å)	b (Å)	c (Å)
Monolayer	4.57	3.31	—
Bilayer	4.51	3.32	—
Trilayer	4.48	3.32	—
Bulk	4.43	3.32	10.47
Exp[a]	4.38	3.31	10.48

[a]Data taken from x-ray diffraction experiments of Ref. [52].

Brillouin zone (BZ) [see Fig. 1(e)], which is calculated to be 1.55, 1.05, and 0.77 eV for one, two, and three monolayers of BP, respectively, and drops down to 0.28 eV in the bulk. The band structure of monolayer BP is evidently similar to the one obtained as the number of monolayers increases as seen in Figs. 2(b) and 2(c), even though extra split bands appear because of the electronic confinement along the z direction. In the bulk limit, the electronic structure of the conventional cell is displayed in Fig. 2(d) for a rectangular path taken at $k_z = 0$ in a reciprocal space that is equivalent to the projection of the bulk BZ along the interlayer direction [see also Figs. 1(d) and 1(e)]. Given that the direction along which we observe the interlayer dispersion (ΓZ) is doubled in the primitive compared to the conventional cell, the back-folded bands in the band structure of the conventional setup in Fig. 4(d) outline the binding energy range in which a band in the primitive cell disperses as we are moving along the ΓZ high-symmetry direction. Hence, the information of the band structure in Figs. 2(d)–2(h) would be virtually equivalent to the combination of band dispersions for $k_z = 0$ (Γ) and $k_z = \frac{\pi}{c}$ (Z) in the primitive reciprocal cell of Fig. 1(d).

The corresponding dispersions are drawn for the basal high-symmetry directions and compared to the experimental data in Fig. 3. In Figs. 2(e)–2(h) the orbital character of the band structure of BP in the conventional cell is presented, stressing that the orbital profile does not change down to the BP monolayer. The bands close to the Fermi level, and also the bottom of the conduction band, have predominantly a p_z character with contribution from s and p_x orbitals, while the orbitals along the zigzag high-symmetry direction (i.e., p_y) are not contributing at the top (bottom) of the valence (conduction) band. The calculated orbital decomposition of the band structure is consistent with theoretical studies employing different methodologies [43,51].

In Fig. 3 high-resolution ARPES spectra along $\bar{\Gamma}\bar{X}$ and $\bar{\Gamma}\bar{Y}$ high-symmetry directions are overlaid by theoretical calculations in the primitive cell of bulk BP [see Fig. 1(d)] for planes in the reciprocal space parallel to k_z axis containing the Γ ($k_z = 0$) and Z ($k_z = \frac{\pi}{c}$) points, which correspond to the red and blue dashed lines, respectively. The theoretical predictions about the orbital character of the band structure can be checked for consistency using ARPES taking into account the light polarization and experimental geometry. We have to stress that only a qualitative comparison is possible given that ground-state DFT calculations do not consider intensity modulations due to matrix-element effects. In Fig. 3(a) the $\bar{\Gamma}\bar{X}$ is probed when HP light impinges the sample along the $\bar{\Gamma}\bar{Y}$ high-symmetry direction, thus enhancing the sensitivity to s, p_y, and p_z orbitals. The results of Fig. 3(b) were obtained by rotating the sample toward the incident HP light by changing the angle ω accordingly, thus enhancing the contribution from p_y orbitals. This is consistent with the observed increase in the spectral weight between 3 and 5 eV below the Fermi energy (E_F) near the $\bar{\Gamma}$ point, which is due to the predominant contribution from p_y orbitals. As seen in Fig. 3(c), switching
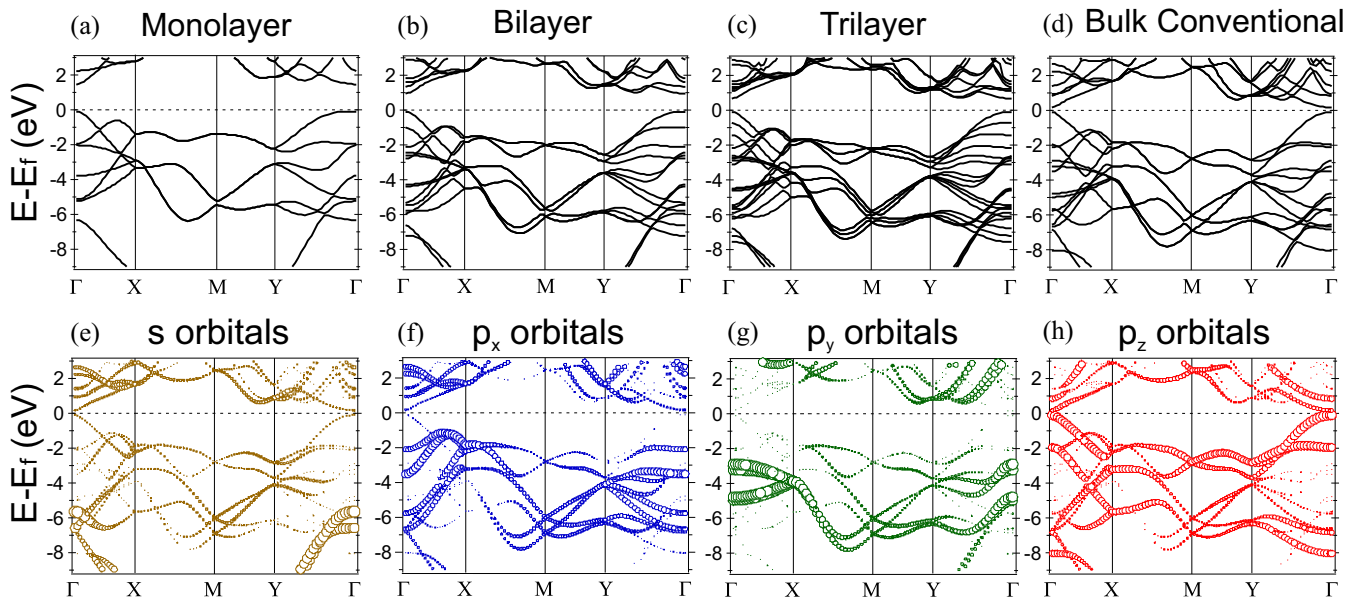
FIG. 2. Electronic structure calculations of (a) monolayer, (b) bilayer, (c) trilayer, and (d) bulk BP in the conventional setup using hybrid functionals. Orbital-projected band structure of bulk BP where (e) brown, (f) blue, (g) green, and (h) red symbols correspond to s, p_x, p_y, and p_z orbitals, respectively. In the orbital-decomposed graphs the size of the symbol is proportional to the orbital's weight contribution to the total wave function.
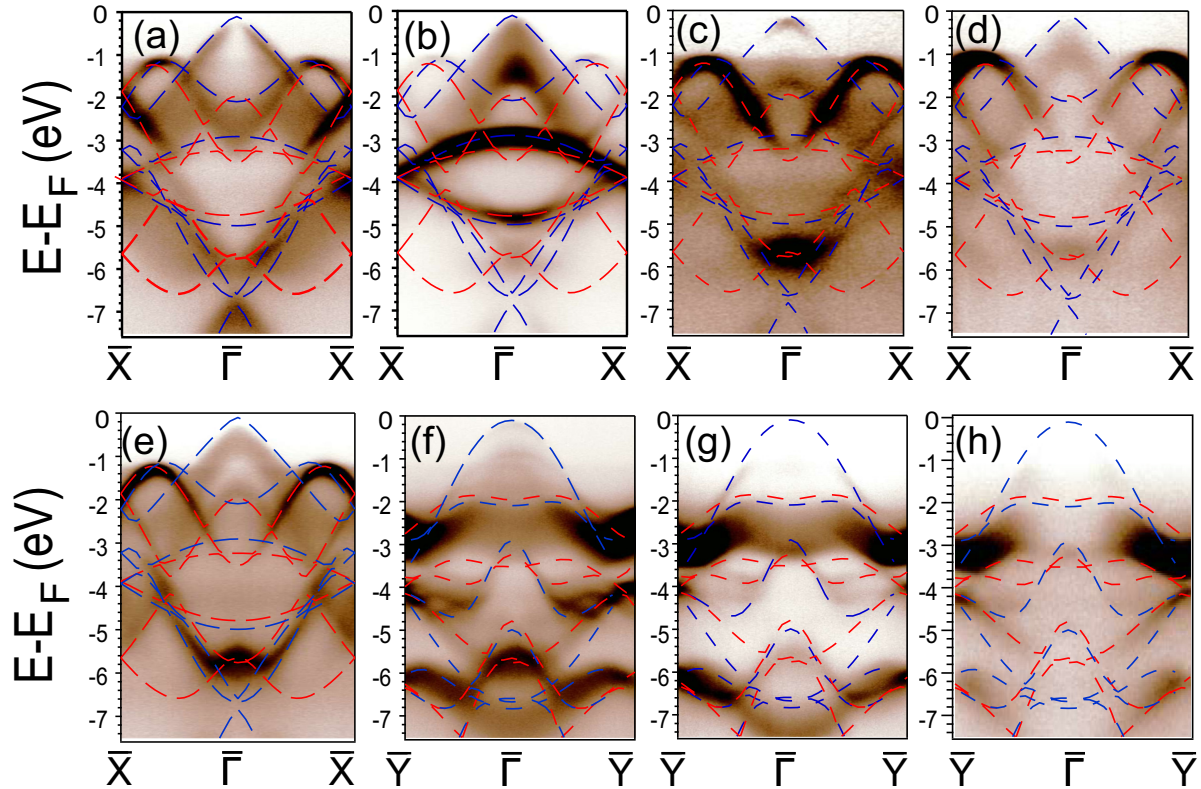
FIG. 3. High-resolution ARPES dispersions around the $\bar{\Gamma}$ point of the surface BZ as measured using HP light along $\bar{\Gamma}\bar{X}$ high-symmetry direction using a photon energy of $h\nu = 104$ eV while probing (a) the first and (b) the second BZ of BP. Photoemission spectra acquired along the $\bar{\Gamma}\bar{X}$ high-symmetry direction using VP light and excitation energies of (c) $h\nu = 104$ eV, (d) $h\nu = 80$ eV, and (e) $h\nu = 90$ eV. ARPES spectra taken along the $\bar{\Gamma}\bar{Y}$ high-symmetry direction using HP light and photon energies of (f) $h\nu = 104$ eV and (g) $h\nu = 80$ eV. (h) High-resolution ARPES dispersion along the $\bar{\Gamma}\bar{Y}$ high-symmetry direction using VP light and a photon energy of $h\nu = 90$ eV. In all spectra, the calculated band dispersions using the hybrid functional method are overlaid. Red (blue) dashed lines correspond to energy dispersions along bulk high-symmetry planes with $k_z = 0$ ($k_z = \frac{\pi}{c}$) in the primitive cell of Fig. 1(d).

the light to VP and with an incidence angle of $\omega \approx 45°$, results in an increased contribution from p_x orbitals in agreement with the increasing intensity observed for the hole-like band near the $\bar{X}$ point with its apex locate at ~ 1 eV below E_F as observed in Figs. 3(c)–3(e). On the other hand, rotating the sample in order to align the incidence plane along the $\bar{\Gamma}\bar{X}$ high-symmetry direction and using HP light increases the spectral weight from p_x and p_z orbitals, a fact that is in agreement with the spectra of Figs. 3(f) and 3(g). Note that switching to VP light the contribution from p_y orbitals is enhanced and as a result the intensity is lowered across the whole spectrum compared to the HP case. Overall, the experimental results support qualitatively our theoretical calculations regarding the orbital character of the different bands, and the calculated band dispersions are in good agreement with the experimentally observed ones. By changing the incident photon energy in Figs. 3(a)–3(e), we clearly observe the dispersion of the bulk bands along the k_z direction (momentum perpendicular to the surface), especially near the top of the valence band at the $\bar{\Gamma}$ point. Moreover, we observe in the experimental spectra of Fig. 3 a large band broadening. For example, in Figs. 3(a) and 3(b) the parabolic band between 2 and 3 eV binding energy and the hole-like band between 2 eV and E_F, which are both centered at the $\bar{\Gamma}$ point, respectively, have spectral weight between the

calculated boundaries where the bands of bulk BP are predicted to disperse. This effect has been also observed in other layered structures, like TMDs, and has been ascribed to the convolution of different k_z values in the same spectrum [53].

The intralayer dispersions as observed in our high-resolution ARPES spectra along the armchair and zigzag directions are consistent with our DFT calculations. The interlayer band dispersion, which is linked to the charge localization, is probed by changing the excitation energy, light polarization, and sample orientation. In Fig. 4(a) we observe the bulk dispersion of the top valence band at the $\bar{\Gamma}$ of the surface BZ in a full period in the k_z direction using VP light incident along the $\bar{\Gamma}\bar{Y}$ direction. We observe that the band has a minimum at approximately 80 and 130 eV and a maximum at 104 eV. In order to determine the component of the electron momentum perpendicular to the surface, $k_\perp$, we estimated the inner potential V_o, which represents the difference in kinetic energy between the measured and free electron-like final state in the solid. Fitting the periodicity of the band B_1 as shown in Fig. 4(a) between Γ and Z in the primitive cell ($k_{\Gamma Z} \approx 0.6$ Å^{-1}) we obtain $V_o = 17.3$ eV, a value that is very close to the bottom of the valence band of BP located at 18.4 eV below the vacuum level, in agreement with previous experimental studies [40]. Although there is an error in the k_z
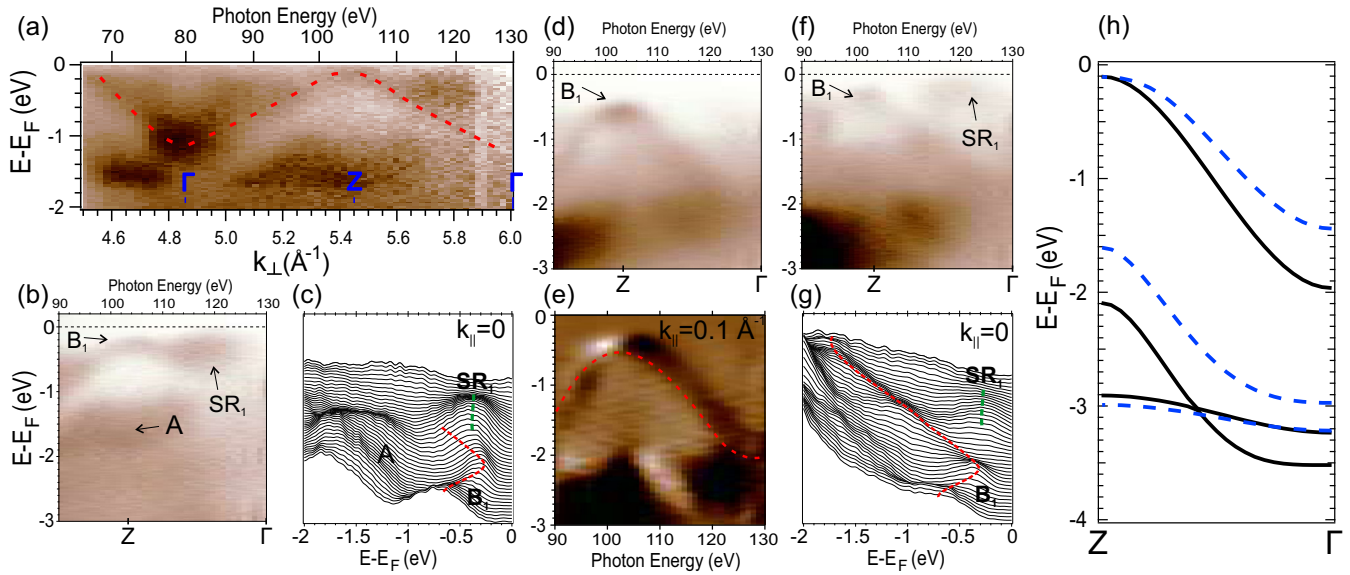
FIG. 4. (a) Band dispersion along the k_z direction of the electronic states at the $\bar{\Gamma}$ point of the surface BZ of BP using VP light. The analyzer slit is aligned along the $\bar{\Gamma}\bar{X}$ high-symmetry direction and the excitation energy ranges from 66 to 130 eV spanning more than one full period in k_z over the bulk primitive cell. (b) Close-up into the energy range from 90 to 130 eV at $\bar{\Gamma}$ point using VP light with the analyzer slit aligned along the $\bar{\Gamma}\bar{X}$ high-symmetry direction and the (c) corresponding energy-distribution curves. (d) Band dispersion along the k_z direction of the electronic states at $k_\parallel = 0.1$ Å^{-1} as measured along the $\bar{\Gamma}\bar{X}$ high-symmetry direction using HP light and (e) the first derivate over the energy range shown in (d). (f) Band dispersion along the k_z at $\bar{\Gamma}$ taken along the $\bar{\Gamma}\bar{Y}$ direction using HP light and (g) the corresponding energy-distribution curves. (h) Energy dispersions of bulk BP in the primitive cell setup along the bulk high-symmetry line between Γ and Z as calculated using a semilocal (blue dashed lines) and hybrid functional (black solid lines).

determination due to the uncertainty in V_o, the $k_\perp$ resolution in our experiment is dominated by the intrinsic broadening in the interlayer direction [54], which is an essential effect in the photoemission process. This uncertainty is inversely proportional to the escape depth of the electrons λ ($\delta k = \lambda^{-1}$) and despite the fact that the universal curve of the inelastic mean free path has its minimum in the excitation energy range between 30 and 100 eV [55], in the case of BP the inelastic mean free path [56] in the aforementioned energy range has a mean value above 5 Å, thus resulting in a $k_\perp$ resolution of about 30% of the distance between Γ and Z. Note that a degradation of the bulk band dispersions along the k_z direction would be expected to occur when this value exceeds 50% [54]. Hence, we are still in the band structure regime [54] and despite the apparent band broadening we can nevertheless identify the band positions and the corresponding dispersions, which is evident in the spectra of Fig. 4. Using the estimated value of the inner potential we find that the top of the valence band (marked as B_1) has a maximum at the Z point of the bulk BZ, which agrees well with our DFT calculations shown in Fig. 4(h). We have to stress that in the analysis of the calculated bulk band dispersions perpendicular to the basal plane, the BZ of the primitive cell [see Fig. 2(d)] should be considered, otherwise, the band-folding in the usually employed conventional setup would result in an assignment of the position of the valence-band maximum at the Γ point of the bulk BZ [57]. Experimentally, using VP light we observe that the top of the valence band is dispersing down to ~1.2 eV in Fig. 4(a), where the band B_1 is probed over the whole period of the bulk primitive BZ. A notable difference between

theory and experiment, which has been recently reported by Han and coworkers [42], is the band splitting observed in the binding energy range down to ~1.8 eV. Although the bandwidth observed in our measurements is significantly larger, it is evident from Figs. 4(b) and 4(c) that there is also a second band (labeled A) with small bandwidth and a dispersion centered around 1.6 eV below E_F. In Fig. 4(d), we follow the band dispersion of B_1 using HP light at off-normal angles to circumvent its apex suppression at the $\bar{\Gamma}$ point due to matrix-element effects. We observe that the band B_1 disperses down to ~2 eV below E_F where it merges with a smeared background signal. The dispersion of B_1 is better resolved in Fig. 4(e), where the first derivative with respect to energy enhances the band dispersion while the band A is not visible at binding energies down to 2 eV in the whole photon-energy range. Note that the state A disappears when the light polarization is switched to HP. In addition, we probed the dispersion at $k_\parallel = 0$ after aligning the incidence plane along $\bar{\Gamma}\bar{X}$ and the resulting spectra are shown in Figs. 4(f) and 4(g). We observe from the energy-distribution curves of Fig. 4(g) that the minimum of the B_1 band dispersion reaches ~1.7 eV binding energy with a similar dispersion as the one observed in Fig. 4(d), taking into account that off-normal emission moves the minimum of the hole-like band toward higher binding energies [see Figs. 4(d) and 4(e)]. This conclusion is similar to the one from Takahashi and coworkers [40]. Furthermore, we stress that the theoretical bandwidth as seen in Fig. 4(h) is ~1.4 eV when using only the semilocal functional (blue-dashed lines), while it increases to about 1.8 eV when a portion (25%) of exact exchange is added to the calculation (solid black

lines). Hence, the experimental bandwidth is closer to the calculated value if exact exchange is included, a methodology that in addition predicts more accurately the bulk band gap of BP. This is expected as the size of the bulk band gap and the exact bandwidth are both related to the strength of the interlayer interaction [44]. Moreover, the bandwidth of the valence band is a manifestation of electronic delocalization perpendicular to the basal plane, which is in accordance with recent transport [58] and Raman spectroscopy [59] studies, indicating that monolayers in bulk BP are strongly coupled, which results in carrier delocalization along the k_z axis. One question that remains to be answered is what is the origin of the state A, which appears when we probe the k_z dispersion using VP light along the $\bar{\Gamma}\bar{Y}$ direction. The most probable explanation is a complex interplay between matrix-element and final-state effects known as secondary cone emission [60]. Strocov *et al.* [61,62] have shown that in layered structures like TMDs where final states deviate strongly from the free-electron-like behavior, the accessibility to multiple final states in a narrow energy range above the Fermi level can lead at one given photon energy to the appearance of contributions from different $k_\perp$ values in the same spectrum. The above-mentioned phenomenon is not limited to layered structures but has been also observed in metallic systems such as Bi(111) [63]. To verify this explantation we have calculated the electronic structure above E_F for bulk BP and compare it to the one of Al, Si, and Ag to qualitatively understand the final states of bulk BP (see Supplemental Material [64]). Our results show that the complexity and multiplicity of upper bands in bulk BP is pronounced and can be linked with the observed features not predicted in the DFT calculations.

Finally, our calculations allow us to disentangle surface from bulk contributions by examining the charge localization in a slab configuration, which has been successfully used to identify surface states and resonances in a variety of materials from metals [65] to layered materials held together by VdW forces like topological insulators [66]. In order to identify states that are localized at the surface, we employed an 11-layer BP slab with more than 20 Å separating consecutive slab images due to periodic boundary conditions. The electronic wave functions at a given energy and $k_\parallel$ were projected to spherical harmonics around the slab ions. In Fig. 5(a), blue circles mark states that have more than 50% of their weight in one of the opposite surfaces of the BP slab. The layered nature of BP and the weak VdW interaction between monolayers can lead to localization of electronic states in the bulk region. To identify states that are not localized at the surface, but can be confined in a monolayer in the bulk region, we applied the same criterion in the middle layers of the slab. The resulting states are marked with blue circles in Fig. 5(b). States that are located only at the surface and experimentally studied in the present work are labeled correspondingly in Fig. 5 (SR_1 to SR_4). We emphasize that the overlap of these surface localized bands with bulk states near the border of the gap, as one can also observe in the experimental data of Fig. 4, classifies these states as surface resonances.

We can now link the theoretical predictions with our experimental observations. In Figs. 4(b) and 4(f), using different polarizations and sample orientations, we notice a dispersionless feature (SR_1) in the photon-energy range
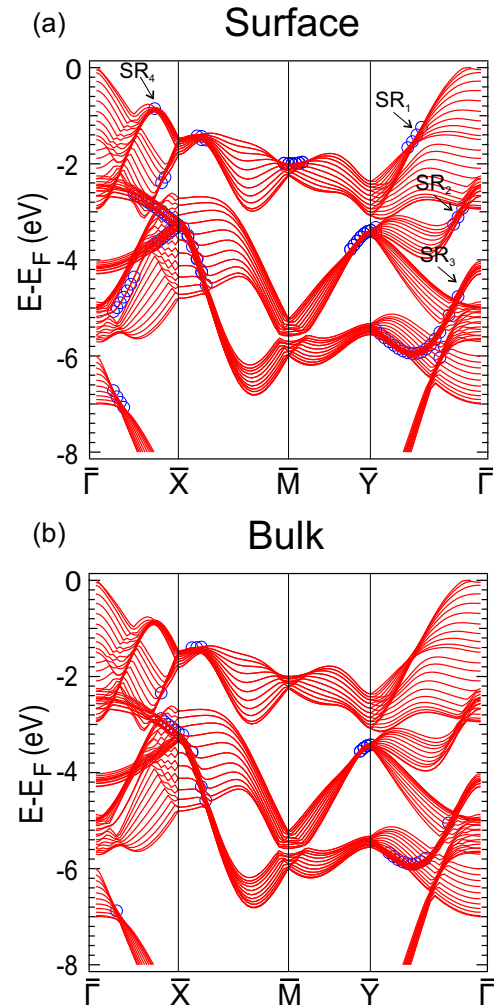
FIG. 5. Calculated band structure using a semilocal functional (PBE) of a BP symmetric slab composed of 11 layers. Blue circles mark states at a given binding energy and $k_\parallel$ value where the wave function projection onto spherical harmonics around the phosphorus atoms of the surface layers exceeds 50% of the total weight (a) on the surface and (b) in the bulk of the slab.

between 110 and 130 eV. This surface resonance appears when the bulk band B_1 disperses toward higher binding energies and despite the diffused broadened signal its spectral weight maximum is not changing with the modulation of the excitation energy as it is evident from the energy distribution curves of Fig. 4(c) and 4(g). In Fig. 6(a), where the experimental band dispersion along $\bar{\Gamma}\bar{Y}$ is displayed, we mark with dotted lines the surface resonances identified by the DFT calculations shown in Fig. 5. In Fig. 6(b) we observe the dependence of SR_2 and SR_3 while changing the excitation energy, states that have a very small dispersion perpendicular to the surface, indicating their 2D localization. In Fig. 6(c), we zoom in around the region near the Fermi level, where the surface resonance SR_1 appears like a rim around the smeared background signal of the bulk bands. It is clear from Fig. 6(d) that SR_1 exhibits a similar behavior with the photon energy. We can also observe this state near the Fermi level when the analyzer slit is aligned along the $\bar{\Gamma}\bar{X}$ direction in Fig. 6(f). In this case, its intensity is suppressed below $\sim$110 eV due to matrix-element effects. Our
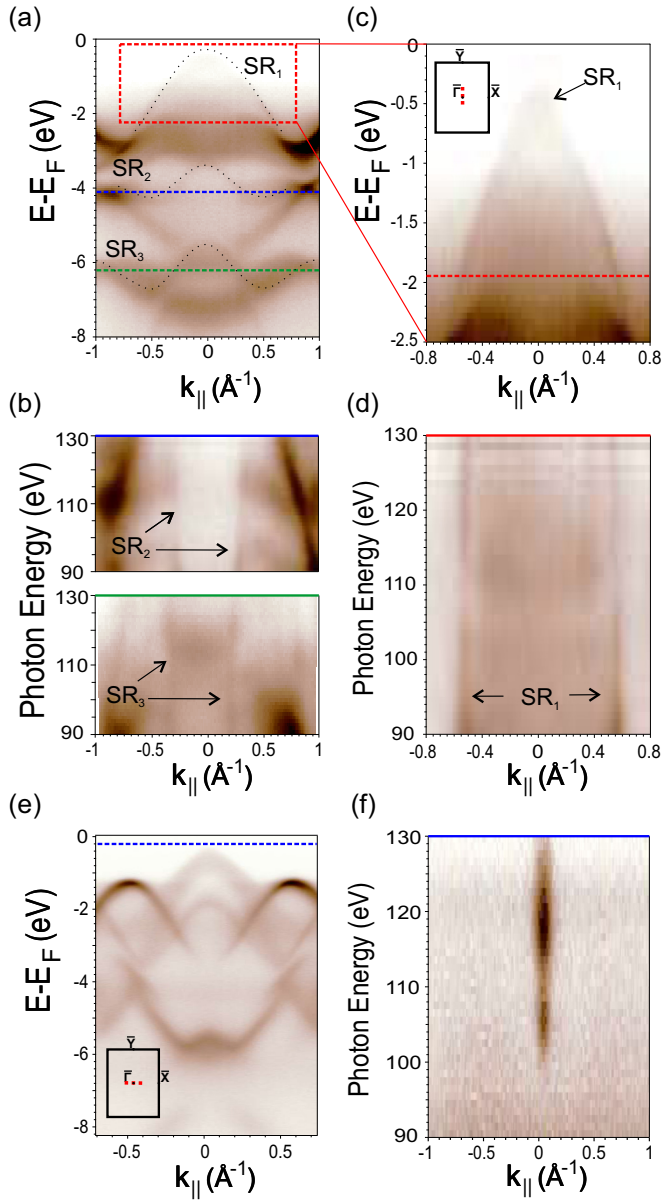
FIG. 6. (a) High-resolution ARPES dispersions along the $\bar{\Gamma}\bar{Y}$ high-symmetry direction using HP light and a photon energy of $h\nu = 104$ eV. Black-dotted lines are guides to the eye for the surface-resonant states. (b) Photon-energy dependence of the SR_2 and SR_3 states at binding energies of 4.1 and 6.2 eV as indicated in (a) by dashed blue and green lines, respectively. (c) Focus on the SR_1 surface-resonance state which is enclosed in the red box in (a). The inset indicates the orientation of the analyzer slit during the measurement by a red-dashed line. (d) Photon-energy dependence of the SR_1 state at binding energy of 1.95 eV marked in (c) by a red-dashed line. (e) High-resolution ARPES dispersion using HP light and a photon-energy of $h\nu = 90$ eV along the high-symmetry direction illustrated using a red-dashed line in the inset. (f) Photon-energy dependence of the SR_3 at a binding energy of 1.95 eV as marked with blue-dashed line in (e).

FIG. 7. (a) High-resolution ARPES spectrum near the $\bar{X}$ point of the surface BZ measured along the line indicated be the red-dashed line in the inset, where a sketch of the surface BZ is shown. Measurements are acquired using HP light and a photon energy of $h\nu = 90$ eV. (b) Momentum-distribution curves extracted at binding energies of 1.1 eV (red), 0.92 eV (blue), 0.54 eV (black), and 0.3 eV (green) corresponding to the colored marks in (a). (c) Energy-distribution curve at (a) $k_{\parallel} = 0$. B_2 and SR_4 mark the bulk and surface-resonant states, respectively. (d) Photon-energy dependence of the SR_4 state at $k_{\parallel} = 0$ and a binding energy of 0.54 eV.

observations along with our theoretical calculations support the existence of surface-resonant states at the $\bar{\Gamma}$ point of the surface BZ. The state that is more relevant to transport and optical applications, which is centered at the $\bar{\Gamma}$ point close to E_F, namely SR_1, is likely to be the one reported using scanning tunneling microscopy [67]. In particular, its relatively narrow line width and the agreement of its energy-momentum dispersion with the calculations indicates that the contribution from impurity states and thus disorder play a minor role. We point out that the line width of this state as obtained from our ARPES experiments cannot be directly compared to the scattering rates extracted from transport measurements, as in our case scattering in all directions strongly contributes to the measured line width.

We have also seen in Fig. 5 that there is a localized state at the surface near the $\bar{X}$ point of the surface BZ, which is also not localized in a monolayer away from the BP slab surface. The difficulty of disentangling this surface contribution from the bulk one near the $\bar{X}$ point of the surface BZ stems from its low intensity and the proximity to a bulk-like state near the $\bar{X}$ point as one can see in Fig. 7(a) (B_2). In Fig. 7(a), the surface-resonant state located at the $\bar{X}$ point is observed above the bulk state B_2 in a saturated high-resolution ARPES spectrum. Figure 7(b) displays the corresponding momentum-distribution curves extracted at different binding energies. We clearly observe that the spectral weight of the surface-resonant state SR_4 is well above the apex of the bulk band B_2 [see red mark in Fig. 7(a)]. This is further corroborated by the energy-distribution curve centered at $k_{\parallel} = 0$ shown in Fig. 7(c), where we can observe the contribution from SR_4 well above the tail

of the spectral weight of the bulk state B_2. Finally, Fig. 7(d) displays the dispersionless surface resonance SR_4, which is visible, although with low relative spectral weight, across a wide range of photon energies.

To summarize, we have employed high-resolution ARPES to investigate the electronic band structure of BP. We find good agreement between the experimentally obtained band dispersions and our DFT calculations. Moreover, by tuning the excitation energy, light polarization, and sample orientation, we probed the interlayer band dispersion of bulk BP. Despite the complexity originating from the existence of multiple final states, our observations confirm the physical picture of interlayer coupling that arises from simple ground-state calculations. Finally, we have theoretically and experimentally identified the existence of strong contributions from surface-resonant states allowing us to disentangle the bulk from the surface contributions in the electronic structure of BP. Our results suggest that surface resonances near the Fermi level could play a key role in the transport and optical properties of BP, a fact that is of critical importance in the context of developing BP-based nanoelectronic devices.

ACKNOWLEDGMENTS

[1] K. S. Novoselov, A. K. Geim, S. V. Morozov, D. Jiang, Y. Zhang, S. V. Dubonos, I. V. Grigorieva, and A. A. Firsov, Science **306**, 666 (2004).

[2] A. K. Geim and K. S. Novoselov, Nature Mater. **6**, 183 (2007).

[3] K. S. Novoselov, A. K. Geim, S. V. Morozov, D. Jiang, M. I. Katsnelson, I. V. Grigorieva, S. V. Dubonos, and A. A. Firsov, Nature **438**, 197 (2005).

[4] K. S. Novoselov, D. Jiang, F. Schedin, T. J. Booth, V. V. Khotkevich, S. V. Morozov, and A. K. Geim, Proc. Natl. Acad. Sci. USA **102**, 10451 (2005).

[5] A. K. Geim and I. V. Grigorieva, Nature **499**, 419 (2013).

[6] A. H. Castro Neto, N. M. R. Peres, K. S. Novoselov, and A. K. Geim, Rev. Mod. Phys. **81**, 109 (2009).

[7] S. Das Sarma, S. Adam, E. H. Hwang, and E. Rossi, Rev. Mod. Phys. **83**, 407 (2011).

[8] B. Radisavljevic, M. B. Whitwick, and A. Kis, ACS Nano **5**, 9934 (2011).

[9] Q. H. Wang, K. Kalantar-Zadeh, A. Kis, J. N. Coleman, and M. S. Strano, Nature Nanotech. **7**, 699 (2012).

[10] G. Fiori, F. Bonaccorso, G. Iannaccone, T. Palacios, D. Neumaier, A. Seabaugh, S. K. Banerjee, and L. Colombo, Nature Nanotech. **9**, 768 (2014).

[11] D. Jariwala, V. K. Sangwan, L. J. Lauhon, T. J. Marks, and M. C. Hersam, ACS Nano **8**, 1102 (2014).

[12] X. Xu, W. Yao, D. Xiao, and T. F. Heinz, Nature Phys. **10**, 343 (2014).

[13] B. Radisavljevic, A. Radenovic, J. Brivio, V. Giacometti, and A. Kis, Nat. Nanotech. **6**, 147 (2011).

[14] S. Das, H.-Y. Chen, A. V. Penumatcha, and J. Appenzeller, Nano Lett. **13**, 100 (2013).

[15] H. Fang, S. Chuang, T. C. Chang, K. Takei, T. Takahashi, and A. Javey, Nano Lett. **12**, 3788 (2012).

[16] H. O. H. Churchill and P. Jarillo-Herrero, Nature Nanotech. **9**, 330 (2014).

[17] X. Ling, H. Wang, S. Huang, F. Xia, and M. S. Dresselhaus, Proc. Natl. Acad. Sci. USA **112**, 4523 (2015).

[18] I. Shirotani, J. Mikami, T. Adachi, Y. Katayama, K. Tsuji, H. Kawamura, O. Shimomura, and T. Nakajima, Phys. Rev. B **50**, 16274 (1994).

[19] A. S. Rodin, A. Carvalho, and A. H. Castro Neto, Phys. Rev. Lett. **112**, 176801 (2014).

[20] R. Fei, V. Tran, and L. Yang, Phys. Rev. B **91**, 195319 (2015).

[21] J. Kim, S. S. Baik, S. H. Ryu, Y. Sohn, S. Park, B. G. Park, J. Denlinger, Y. Yi, H. J. Choi, and K. S. Kim, Science **349**, 723 (2015).

[22] Q. Liu, X. Zhang, L. B. Abdalla, A. Fazzio, and A. Zunger, Nano Lett. **15**, 1222 (2015).

[23] H. Du, X. Lin, Z. Xu, and D. Chu, J. Mater. Chem. C **3**, 8760 (2015).

[24] L. Liang, J. Wang, W. Lin, B. G. Sumpter, V. Meunier, and M. Pan, Nano Lett. **14**, 6400 (2014).

[25] J. Qiao, X. Kong, Z.-X. Hu, F. Yang, and W. Ji, Nat. Commun. **5**, 4475 (2014).

[26] R. W. Keyes, Phys. Rev. **92**, 580 (1953).

[27] D. Warschauer, J. Appl. Phys. **34**, 1853 (1963).

[28] Y. Maruyama, S. Suzuki, K. Kobayashi, and S. Tanuma, Physica B+C **105**, 99 (1981).

[29] Y. Cai, G. Zhang, and Y.-W. Zhang, Sci. Rep. **4**, 6677 (2014).

[30] V. Tran, R. Soklaski, Y. Liang, and L. Yang, Phys. Rev. B **89**, 235319 (2014).

[31] F. Xia, H. Wang, and Y. Jia, Nat. Commun. **5**, 4458 (2014).

[32] S. P. Koenig, R. A. Doganov, H. Schmidt, A. H. Castro Neto, and B. Özyilmaz, Appl. Phys. Lett. **104**, 103106 (2014).

[33] Y. Du, H. Liu, Y. Deng, and P. D. Ye, ACS Nano **8**, 10035 (2014).

[34] L. Li, Y. Yu, G. J. Ye, Q. Ge, X. Ou, H. Wu, D. Feng, X. H. Chen, and Y. Zhang, Nat. Nanotech. **9**, 372 (2014).

[35] H. Liu, A. T. Neal, Z. Zhu, Z. Luo, X. Xu, D. Tománek, and P. D. Ye, ACS Nano **8**, 4033 (2014).

[36] H. Lüth, *Solid Surfaces, Interfaces and Thin Films*, 4th ed. (Springer, Berlin, 2001).

[37] V. Tayari, N. Hemsworth, I. Fakih, A. Favron, E. Gaufrès, G. Gervais, R. Martel, and T. Szkopek, Nat. Commun. **6**, 7702 (2015).

[38] L. Li, G. J. Ye, V. Tran, R. Fei, G. Chen, H. Wang, J. Wang, K. Watanabe, T. Taniguchi, L. Yang, X. H. Chen, and Y. Zhang, Nat. Nanotech. **10**, 1 (2015).

[39] N. Gillgren, D. Wickramaratne, Y. Shi, T. Espiritu, J. Yang, J. Hu, J. Wei, X. Liu, Z. Mao, K. Watanabe, T. Taniguchi, M. Bockrath, Y. Barlas, R. K. Lake, and C. N. Lau, 2D Materials **2**, 011001 (2014).

[40] T. Takahashi, N. Gunasekara, H. Ohsawa, H. Ishii, T. Kinoshita, S. Suzuki, T. Sagawa, H. KATO, T. Miyahara, and I. Shirotani, Phys. Rev. B **33**, 4324 (1986).

[41] H. Asahina, Y. Takao, and A. Morita, J. Phys. Soc. Jpn **51**, 1193 (1982).

[42] C. Q. Han, M. Y. Yao, X. X. Bai, L. Miao, F. Zhu, D. D. Guan, S. Wang, C. L. Gao, C. Liu, D. Qian, Y. Liu, and J.-F. Jia, Phys. Rev. B **90**, 085101 (2014).

[43] Y. Takao, H. Asahina, and A. Morita, J. Phys. Soc. Jpn **50**, 3362 (1981).

[44] A. Morita, Appl. Phys. A **39**, 227 (1986).

[45] N. B. Goodman, L. Ley, and D. W. Bullett, Phys. Rev. B **27**, 7440 (1983).

[46] HQ Graphene, www.hqgraphene.com.

[47] P. E. Blöchl, Phys. Rev. B **50**, 17953 (1994).

[48] J. P. Perdew, K. Burke, and M. Ernzerhof, Phys. Rev. Lett. **77**, 3865 (1996); **78**, 1396 (1997).

[49] S. Grimme, J. Comp. Chem. **27**, 1787 (2006).

[50] J. Heyd, G. E. Scuseria, and M. Ernzerhof, J. Chem. Phys. **118**, 8207 (2003); **124**, 219906 (2006).

[51] A. N. Rudenko, S. Yuan, and M. I. Katsnelson, Phys. Rev. B **92**, 085419 (2015).

[52] A. Brown and S. Rundqvist, Acta Cryst. **19**, 684 (1965).

[53] D. W. Latzke, W. Zhang, A. Suslu, T.-R. Chang, H. Lin, H.-T. Jeng, S. Tongay, J. Wu, A. Bansil, and A. Lanzara, Phys. Rev. B **91**, 235202 (2015).

[54] V. N. Strocov, J. Electron. Spectrosc. Relat. Phenom. **130**, 65 (2003).

[55] S. Hüfner, *Photoelectron Spectroscopy* (Springer-Verlag, Berlin, 1996).

[56] C. J. Powell and A. Jablonski, *NIST Electron Inelastic-Mean-Free-Path Database* (National Institute of Standards and Technology, Gaithersburg, MD, 2010).

[57] Y. Du, C. Ouyang, S. Shi, and M. Lei, J. Appl. Phys. **107**, 093718 (2010).

[58] D. J. Perello, S. H. Chae, S. Song, and Y. H. Lee, Nat. Commun. **6**, 7809 (2015).

[59] X. Luo, X. Lu, G. K. W. Koon, A. H. Castro Neto, B. Özyilmaz, Q. Xiong, and S. Y. Quek, Nano Lett. **15**, 3931 (2015).

[60] G. D. Mahan, Phys. Rev. B **2**, 4334 (1970).

[61] V. N. Strocov, H. I. Starnberg, P. O. Nilsson, H. E. Brauer, and L. J. Holleboom, Phys. Rev. Lett. **79**, 467 (1997).

[62] V. N. Strocov, E. E. Krasovskii, W. Schattke, N. Barrett, H. Berger, D. Schrupp, and R. Claessen, Phys. Rev. B **74**, 195125 (2006).

[63] C. R. Ast and H. Höchst, Phys. Rev. B **70**, 245122 (2004).

[64] See Supplemental Material at http://link.aps.org/supplemental/10.1103/PhysRevB.93.075207.

[65] F. J. Arlinghaus, J. G. Gay, and J. R. Smith, Phys. Rev. B **21**, 2055 (1980).

[66] K. Park, J. J. Heremans, V. W. Scarola, and D. Minic, Phy. Rev. Lett. **105**, 186801 (2010).

[67] C. D. Zhang, J. C. Lian, W. Yi, Y. H. Jiang, L. W. Liu, H. Hu, W. D. Xiao, S. X. Du, L. L. Sun, and H. J. Gao, J. Phys. Chem. C **113**, 18823 (2009).